PHYSICAL REVIEW B **85**, 174302 (2012)

Optical decoherence studies of yttrium oxyorthosilicate Y_2SiO_5 codoped with Er^{3+} and Eu^{3+} for optical signal processing and quantum information applications at 1.5 microns

C. W. Thiel[*] and W. R. Babbitt[†]
Spectrum Lab, Montana State University, Bozeman, Montana 59717, USA

R. L. Cone[‡]
Department of Physics, Montana State University, Bozeman, Montana 59717, USA

(Received 30 December 2011; revised manuscript received 17 April 2012; published 11 May 2012)

We report detailed studies of the optical decoherence and spectroscopic properties of the 1536-nm optical transition of the bandwidth-engineered material 0.02%Er:1%Eu:Y_2SiO_5. This work is motivated by the need for comprehensive understanding of new resonant optical materials for spatial-spectral holography and quantum information applications. The dependence of optical decoherence on excitation frequency, applied magnetic field strength and orientation, crystal temperature, measurement time scale, and optical excitation density was studied using stimulated photon echo spectroscopy and time-resolved spectral hole-burning techniques. The effects of weak disorder generated by the introduction of Eu^{3+} ions into the lattice was probed by comparing measurements across the static disorder-induced distribution of transition frequencies as well as by comparing with measurements on 0.02%Er:Y_2SiO_5. The results reveal that the coherence properties of Er:Y_2SiO_5 are preserved in the disordered system; moreover, the increased inhomogeneity produced by the disorder acts to suppress optical decoherence by inhibiting the electronic spin diffusion process, improving material properties for low magnetic field strengths and at increased temperatures desirable for practical applications.

DOI: 10.1103/PhysRevB.85.174302 PACS number(s): 42.50.Md, 76.30.Kg, 42.62.Fi, 42.70.−a

I. INTRODUCTION

The resonant optical material Er^{3+}-doped yttrium oxyorthosilicate (Er:Y_2SiO_5) is one of the most promising known systems for enabling spatial-spectral holography (SSH), spectral hole-burning (SHB) devices, and quantum memory applications. This material system exhibits a number of important properties at liquid-helium temperatures and with an applied magnetic field, including unusually long coherence lifetimes and a nearly oscillator strength limited excited-state lifetime.[1–5] Furthermore, this material operates in the 1.5-μm telecommunication band where extensive low-cost optical hardware has been developed and commercially tested by the telecommunications industry. Er:Y_2SiO_5 materials have been successfully employed in a wide range of demonstrations that include wideband signal processing,[6] all-optical correlators,[7,8] radio-frequency spectral analysis,[9] laser frequency stabilization,[10–12] electromagnetically induced transparency (EIT),[13] ultraslow light propagation,[14] coherent single-photon storage and retrieval,[15] and dynamic spectral filtering.[16] Er:Y_2SiO_5 has also been considered and studied as a potential system for quantum memory applications.[17–21]

It has recently been shown that codoping Er:Y_2SiO_5 with Eu^{3+} ions allows the optical processing bandwidth to be expanded to tens of gigahertz with no negative impact on the coherence properties, resulting in both narrow homogeneous linewidths and broad inhomogeneous absorption lines.[22] In spite of these interesting material attributes, many of the spectroscopic and decoherence properties relevant to applications have not yet been reported for the full range of operating conditions of interest for practical implementations. Specifically, we wish to understand how the material properties vary for low applied magnetic field strengths accessible using simple and compact permanent magnet assemblies ($<$1.5 T), for temperatures achievable with low-vibration closed-cycle cryostats (2–5 K), and for interaction time scales practical for complex signal programming, processing, or readout tasks ($>$100 μs). This parameter space is particularly important for SSH applications such as high-bandwidth spectrum analysis or RADAR signal processing that must ultimately operate under conditions compatible with compact, robust, and deployable hardware.[6–9] These conditions are also relevant to quantum memory demonstration efforts where operation at lower magnetic field strengths can be desirable to minimize spin-lattice relaxation of Er^{3+}.[18,21] This regime of operation can result in much different behavior than the high-field ($>$1 T), low-temperature ($<$2 K) conditions previously studied[1–5] since additional interaction and relaxation mechanisms can become active. While the complexity makes it difficult to apply quantitative theoretical models to describe the observed properties or predict material behavior, fully exploring this rich parameter space offers invaluable insights into the underlying material physics.

To improve our understanding of Er^{3+} materials and material disorder in general, optimize Er:Eu:Y_2SiO_5 materials for optical signal processing applications, and characterize material properties under different operating conditions, extensive material studies have been performed. We report studies of the optical properties and decoherence dynamics of the $^4I_{15/2}(1) \leftrightarrow {}^4I_{13/2}(1)$ transition at 1536 nm for Er^{3+} ions residing at crystallographic site 1 in 0.02%Er:1%Eu:Y_2SiO_5. Optical decoherence was measured using stimulated photon echo spectroscopy as a function of magnetic field strength and orientation, measurement time scale, crystal temperature, and optical excitation density, gaining insight into spectral diffusion and the underlying microscopic spin dynamics

1098-0121/2012/85(17)/174302(15)

responsible for the optical decoherence and spectral broadening of the transition. Additionally, we probed the nature of the inhomogeneous broadening, confirming that ions with resonance frequencies across the broadened absorption line exhibit the same decoherence rates for the conditions studied. Finally, we found that the disorder introduced to increase optical signal processing bandwidth also results in a significant suppression of decoherence by inhibiting the electronic spin diffusion process. Together, the work reported here directly impacts our fundamental understanding of disorder in doped optical materials and contributes to ongoing efforts to design materials with properties tailored to specific applications.

II. Er:Eu:Y_2SiO_5 MATERIALS

The host crystal yttrium oxyorthosilicate Y_2SiO_5 (also known as YSO), is monoclinic and has three orthogonal optical extinction axes: the crystal's **b** axis and the $\mathbf{D}_1$ and $\mathbf{D}_2$ axes that correspond to the two optical extinction directions when the crystal is viewed along the **b** axis between crossed polarizers. The $\mathbf{D}_1$ axis is oriented 23.8° from the crystal's **c** axis and 78.7° from the crystal's **a** axis, and the $\mathbf{D}_2$ axis is orthogonal to $\mathbf{D}_1$ and **b**.[23] The Y^{3+} ions occupy two crystallographically inequivalent sites of C_1 point symmetry referred to as "site 1" and "site 2" and the Er^{3+} and Eu^{3+} ions substitute for Y^{3+} host ions at both sites without charge compensation.[24] The Er^{3+} ionic radius is very similar to that of Y^{3+}, and the occupancy of the two Y^{3+} sites by Er^{3+} dopant ions is believed to be nominally equal, while Eu^{3+} exhibits greater occupation of one site relative to the other due to its larger ionic radius.[25] For each crystallographic site, there are two magnetically inequivalent subclasses of sites with the same local structure but with different relative orientations; however, the two subclasses of a given site become magnetically equivalent when the magnetic field is applied along the **b** axis or within the $\mathbf{D}_1$-$\mathbf{D}_2$ plane.[26] This magnetic equivalency is desirable for applications since it minimizes the number of optical transitions in the spectrum, simplifies the ion-ion interaction dynamics, and increases the optical absorption of each transition. Motivated by these considerations, we focus on the material properties when the magnetic field is applied in the $\mathbf{D}_1$-$\mathbf{D}_2$ plane.

In the work presented here, we study the 1536-nm optical transition of Er^{3+} ions residing at crystallographic site 1. This transition exhibits the strongest absorption when the light is polarized parallel to the $\mathbf{D}_2$ direction.[4,22] For this wavelength and polarization, the results of Beach *et al.*[27] predict an index of refraction of 1.789. The 1536-nm absorption line corresponds to the optical transition from the lowest-energy crystal field level of the $^4I_{15/2}$ ground-state multiplet to the lowest-energy crystal field level of the $^4I_{13/2}$ excited-state multiplet, known as the "1 to 1" transition to indicate that the lowest-energy level of each multiplet is involved. This transition is generally preferred for study and applications since other transitions involving higher energy levels in either multiplet experience additional decoherence due to rapid relaxation to the lowest level within the multiplet through phonon emission. For this work, the site 1 transition was chosen over the site 2 transition at 1539 nm since the site 1 transition offers a larger absorption bandwidth and less spectral diffusion at low magnetic field strengths.[5,22]

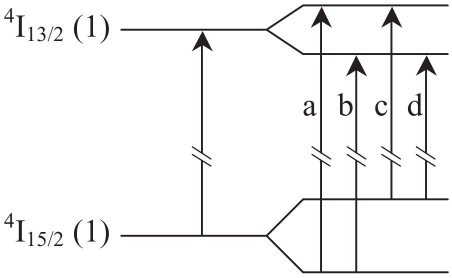

FIG. 1. Illustration of the splitting of Er^{3+} energy levels in an applied magnetic field and the corresponding 1.5-μm optical transitions. The "b" transition is preferred for applications that require low decoherence.

Practical operation of Er^{3+}-doped materials in SSH/SHB devices generally requires the application of an external magnetic field to achieve long coherence times through the suppression of dynamic magnetic dipole-dipole interactions. For paramagnetic centers such as Er^{3+}, time-reversal symmetry requires that each energy level be at least a degenerate doublet composed of time-reversed states. This degeneracy is broken when an external magnetic field is applied through the Zeeman effect so that each energy level splits into "Zeeman sublevels." Consequently, each optical transition splits into four transitions that we label as diagrammed in Fig. 1. Generally, the "*b*-line" optical transition shown in Fig. 1 will offer the minimum decoherence and longest lifetimes since the other three transitions involve higher-energy components with additional relaxation pathways to the lower-energy component. In addition, the *a*-line and *d*-line transitions couple more strongly to the magnetic perturbations in the crystalline environment that cause decoherence. The relative strength of these four transitions depends on both the transition cross sections and the thermal distribution of population between the ground-state sublevels, causing the *c*-line and *d*-line transitions to be weaker at lower temperatures and higher magnetic field strengths where the upper component of the ground-state doublet can become depopulated. Furthermore, if the magnetic field is applied along a direction where the two magnetic subclasses of each site are inequivalent, they will experience different splittings and double the number of absorption lines in the spectrum.

Because of its many desirable properties, the Er^{3+}-doped Y_2SiO_5 material system has received much attention for optical signal processing and quantum information applications that exploit spectral hole burning and optical coherent transients.[6–21] In addition, the long coherence lifetimes have enabled detailed studies of ion-ion and ion-spin interactions that have provided fundamental insights into spectral diffusion with broad impact on understanding decoherence in other paramagnetic materials.[3,5,28] These studies have led to the observation of a homogeneous ensemble linewidth in Er:Y_2SiO_5 as narrow as 73 Hz, the narrowest optical transition known for any impurity in a solid.[2,5]

In many optical signal processing applications and quantum information protocols, the spectral width of the optical transition in the active medium determines the maximum signal bandwidth or information storage density.[29] Consequently, one aspect of Er:Y_2SiO_5 that has limited its use in signal processing applications is the relatively narrow inhomogeneous spectral linewidth of typically only a few hundred megahertz. The inhomogeneous linewidth Γ_{inh} results from a static distribution of ion transition frequencies caused by inhomogeneous strain throughout the crystal lattice. While a narrow distribution of transition frequencies increases the overall absorption and is a beneficial property for some applications such as frequency references, the inhomogeneous linewidth limits the maximum signal bandwidth that may be processed by the material. Motivated by the need to enable high-bandwidth signal processing applications, we have previously increased the inhomogeneous linewidth of Er:Y_2SiO_5 in a controlled manner by codoping with specific levels of Eu^{3+} ions to introduce static disorder into the crystal lattice.[22] The initial measurements on the Er:Eu:Y_2SiO_5 materials demonstrated increased optical bandwidth while still maintaining the other desirable properties of Er:Y_2SiO_5.[22] Beyond that initial report, no other studies of these codoped materials have yet been reported, motivating the work reported here.

III. EXPERIMENTAL DETAILS

The 0.02%Er:1%Eu:Y_2SiO_5 and 0.02%Er:Y_2SiO_5 crystals studied in this work were grown by Scientific Materials, Inc. (Bozeman, Montana) using the Czochralski method. The crystals were x-ray oriented, cut perpendicular to the three optical extinction axes, and polished to optical quality. The orientation of the optical extinction directions $\mathbf{D}_1$ and $\mathbf{D}_2$ with respect to the crystal faces was verified by viewing the crystals between crossed polarizers. All crystals were transparent and appeared colorless. The nominal Er^{3+} and Eu^{3+} concentrations of 0.02% and 1% atomic percent substitution for Y^{3+}, respectively, were specifically chosen to provide a suitable combination of absorption strength ($\sim$1.5 cm^{-1}) and processing bandwidth ($\sim$10 GHz).

All samples were mounted in an Oxford SpectroMag liquid-helium cryostat to provide variable temperatures down to 1.2 K and magnetic field strengths of up to 7 T. Samples were immersed in superfluid liquid helium for temperatures below 2.17 K and in helium gas for higher temperatures. Samples were oriented so that the magnetic field was applied parallel to the $\mathbf{D}_1$-$\mathbf{D}_2$ plane to within ±0.1° by spectrally monitoring the magnetic equivalency of the two subclasses for each site. Alignment of the magnetic field at a specific orientation in the $\mathbf{D}_1$-$\mathbf{D}_2$ plane was achieved to within better than ±0.5° by rotating the crystal within the cryostat using a gear assembly. The laser light used for these studies was generated by two external cavity diode lasers with $\sim$250 kHz linewidth, amplified using an erbium-doped fiber amplifier, and detected using New Focus 1811 amplified InGaAs photodiodes. The laser beam propagated parallel to the **b** axis of the crystals, and the polarization vector of the light was kept parallel to the $\mathbf{D}_2$ extinction axis of the crystals for all measurements. The absolute frequencies of the lasers were monitored using a Burleigh WA-1500 wave meter and calibrated with an $H^{13}C^{14}N$ gas cell frequency reference to better than 100 MHz. An acousto-optic modulator (AOM) gated the laser beam to generate pulses for echo and time-resolved hole-burning measurements. For photon echo measurements, typical pulse lengths of $\sim$60 ns were used to produce $\pi/2$ pulse areas. The optical intensity at the crystal was estimated to be $\sim 3 \times 10^4$ W/cm^2 from the known transition oscillator strength and the Rabi frequency of optical nutation observed for these conditions. A second AOM was placed before the detector to block excitation pulses and selectively pass emitted echo signals or spectral hole scans. Spectral holes were probed with frequency chirps generated by ramping the laser diode current, and transmission through a fiber Fabry-Perot interferometer with a free spectral range of 49.4 MHz was monitored simultaneously to calibrate the frequency chirps.

IV. STATIC DISORDER AND INHOMOGENEOUS BROADENING

The optical absorption spectrum of the site 1 transition of 0.02%Er:1%Eu:Y_2SiO_5 is plotted as the solid line in Fig. 2 for a temperature of 5.0 K, no applied magnetic field, and light polarized parallel to $\mathbf{D}_2$. The absorption spectrum was determined by measuring the transmission of a broadband light source through the crystal using an Ando AQ6317B optical spectrum analyzer with $\sim$2 GHz spectral resolution. For comparison, the measured spectrum of a 0.02%Er:Y_2SiO_5 crystal is also shown by the dashed line, where the linewidth of the absorption peak is instrumentally limited by the resolution of the optical spectrum analyzer. From these measurements, we find that the site 1 transition occurs at a frequency ν_0 of 195 113.7 GHz in 0.02%Er:1%Eu:Y_2SiO_5, shifted to lower frequency by 3.0 GHz relative to 0.02%Er:Y_2SiO_5. The Eu-doped material exhibits a nearly Lorentzian line shape, as expected for inhomogeneous broadening caused by the presence of point defects.[30] Deconvolving the instrumental response function of the optical spectrum analyzer, we find that the transition has a peak absorption coefficient α_0 of 1.5 cm^{-1} and a linewidth full-width at half-maximum Γ_{inh} of 11 GHz. These values are all in excellent agreement with previously reported laser absorption measurements on this material.[22]

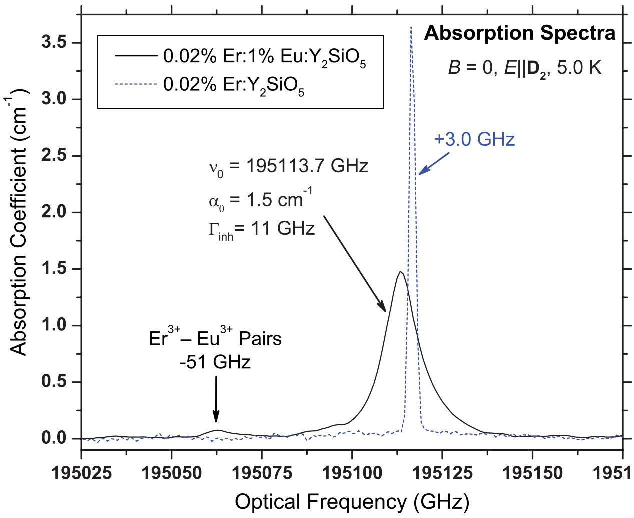

FIG. 2. (Color online) Comparison of absorption spectra of 0.02%Er:1%Eu:Y_2SiO_5 (solid line) and 0.02%Er:Y_2SiO_5 (dashed line). Note that the 0.02%Er:Y_2SiO_5 spectrum is limited by instrumental resolution.

By comparing the spectra in Fig. 2, we note the presence of a weak satellite line that appears in the Eu^{3+}-doped material shifted by 51 GHz to lower frequency relative to the main absorption line. This feature may be attributed to the small fraction of Er^{3+} ions in the lattice that have a neighboring Y^{3+} replaced by a Eu^{3+} ion. Each Er^{3+} ion has two site 1 and two site 2 Y^{3+} nearest neighbors. Therefore, if we assume a perfectly random distribution of dopant ions in the lattice, the Eu^{3+} ions in this crystal have a 1% chance of occupying either of the two equivalent nearest-neighbor Y^{3+} sites for each Er^{3+} ion, so that we expect 2% of the Er^{3+} ions to have nearest-neighbor Eu^{3+} ions at a particular crystallographic site. The integrated absorption line strength of the Er^{3+}-Eu^{3+} pair line observed in the spectrum was ∼2% of the main line's absorption line strength, in agreement with the expected value. The appearance of a single line could indicate overlap of the pair lines for sites 1 and 2 Eu^{3+} neighbors, a very different frequency shift or linewidth for one of the lines, or could be a result of the unequal Eu^{3+} occupation of the two sites. We also expect that some of the structure observed in the tails of the main absorption line results from Er^{3+} ions with more distant Eu^{3+} neighbors. While the studies reported here focus on the main absorption line that corresponds to isolated Er^{3+} ions in the lattice, the Er^{3+}-Eu^{3+} pairs may be of potential interest for applications in quantum information science due to the potential to produce entanglement between the neighboring Er^{3+} and Eu^{3+} ions.[31] For example, this could possibly enable optical operation in the 1.5-μm telecom band through the Er^{3+} absorption while allowing storage of qubits on the long-lived nuclear spin of the Eu^{3+} ion in a spin-bus architecture,[32] or transfer of entanglement between photons resonant with the 1536-nm and 580-nm transitions of the Er^{3+} and Eu^{3+} ions.

Since the enhanced material bandwidth of the Eu^{3+}-doped material results from disorder in the crystal lattice that broadens the optical linewidth, it is important to determine whether Er^{3+} ions with different transition frequencies, corresponding to different local strains and environments, exhibit the same dynamic properties. In addition, when an external magnetic field is applied to suppress decoherence, the *b*-line and *c*-line transitions indicated in Fig. 1 often significantly overlap due to the large inhomogeneous broadening of the transitions. Because of the complex magnetic anisotropy,[26] the degree of overlap for these transitions depends on both the magnetic field strength and orientation. Since both of these transitions can be probed when interrogating the material over its full bandwidth, it is also important to determine if the two transitions exhibit different properties.

To investigate the nature of the increased spectral broadening exhibited by the Eu-doped materials, we performed a series of optical coherence measurements across a 40-GHz span of the absorption line, as shown in Fig. 3. For these measurements, we chose a sample temperature of 1.6 K and applied a magnetic field of $B = 0.5$ T along the crystal's $\mathbf{D}_1$ axis. The measured laser absorption spectrum for these conditions is plotted as the solid line in Fig. 3 for reference. The asymmetric shape of the absorption is due to the overlap of the unresolved *b*-line and *c*-line transitions. For these conditions, the *a*-line transition occurs at 195149.6 GHz, the *b*-line transition is at 195116.8 GHz, the *c*-line transition is at 195110.3 GHz, and the *d*-line transition is at 195077.4 GHz, corresponding to a magnetic splitting of the Er^{3+} ground-state doublet of 39.4 GHz and an excited state splitting of 32.9 GHz. Using those results and Boltzmann statistics for the thermal distribution of population between the two sublevels of the ground state at 1.6 K, we expect that the *c* line should have 22% of the total absorption line strength and that the *b* line should have 78% of the line strength for these conditions, in good agreement with the measured absorption spectrum. To illustrate this, the frequency and relative line strength of the *b* and *c* lines are indicated by the vertical bars in Fig. 3.

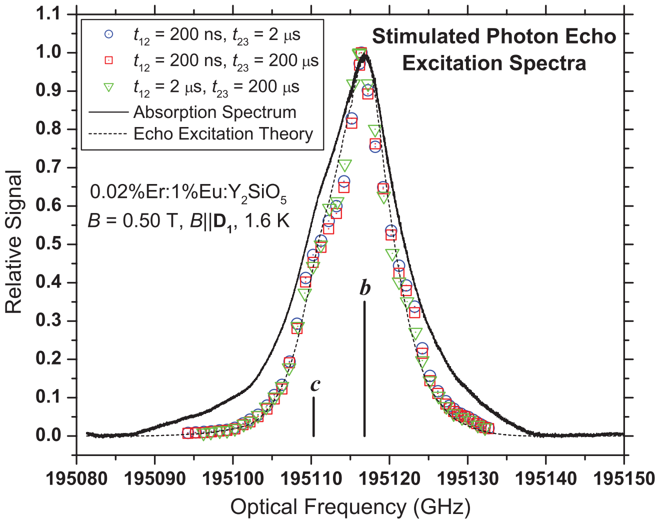

FIG. 3. (Color online) Probe of underlying spectral properties across the absorption line using optical coherence measurements. Measured photon echo intensities (indicated by symbols) reveal that the entire absorption bandwidth and the two overlapping transitions (*b* line and *c* line, indicated by vertical bars representing relative absorption strength) have uniform properties for 0.5 T with $B\|\mathbf{D}_1$ at 1.6 K. The solid line is the measured absorption spectrum and the dashed line is the expected photon echo excitation spectrum calculated from the absorption line shape.

To search for variations in the optical decoherence and homogeneous linewidth of ions distributed across the absorption line, we employed photon echo excitation spectroscopy. In this technique, a series of optical pulses are used to coherently prepare the material and then rephase the stored coherence to generate a "photon echo" of the initial excitation pulse.[33,34] Since the strength of the photon echo depends on the fidelity of the stored coherence, the change in echo intensity as a function of measurement time scale directly probes decoherence due to the intrinsic phase memory lifetime of the optical center as well as decoherence due to time-dependent perturbations from the environment. In photon echo excitation measurements, the measurement time scale is held fixed and the integrated energy of the emitted photon echo is monitored as the frequency is varied across the absorption line. This method is extremely sensitive to the underlying decoherence dynamics at different frequencies so that any change in properties will cause large variations in the shape of the measured excitation spectrum.[35] By using stimulated photon echoes to vary the measurement time scale, the sensitivity of the method may be further increased to probe slow perturbations, weak decoherence, and changes in population relaxation dynamics.[3]

For the photon echo excitation measurements shown by the symbols in Fig. 3, we employed stimulated photon echoes with three different combinations of delay t_{12} between the first and second preparation pulses and delay t_{23} between the second and third pulses. The different combinations of time delays vary the measurement's relative sensitivity to different decoherence and relaxation mechanisms. From the data in Fig. 3, we see that the photon echo excitation spectra are similar to the absorption line shape and are identical for all combinations of time delays, demonstrating that there are no significant variations in properties across the entire material bandwidth.

To further investigate the detailed shape of the echo excitation spectrum, we employed a simple model to calculate the expected spectrum. In this model, we used the first-order approximation for the dependence of the total energy emitted in the photon echo E_{echo} on the transition absorption coefficient α.[33] If we assume a focused laser beam waist in the crystal with a Rayleigh range shorter than the crystal length, as is the case for our measurements, we may describe the variation in E_{echo} across the absorption line α by the relationship

$$E_{\text{echo}} \sim \alpha^2 L^2 e^{-x\alpha L}, \tag{1}$$

where L is the crystal thickness and x is an empirical parameter that depends on the position of the beam waist in the crystal, the Gaussian beam parameters of the laser, the laser intensity, and the excitation pulse widths.[35] The photon echo excitation spectrum calculated from Eq. (1) using a value of $x = 0.5$ and the measured laser absorption spectrum is shown by the dashed line in Fig. 3. The agreement between the model and the observed echo excitation spectra allows us to estimate that the decoherence rates vary by less than ±20% over the entire absorption line for the time scales probed in the different measurements; variations larger than this would result in significant deviations from the model.

In addition to measuring the photon echo excitation spectra shown in Fig. 3, we also measured stimulated photon echo decays for frequencies at the center and both sides of the absorption line. The measured t_{12} decay curves at a fixed t_{23} delay of 200 μs are plotted in the top panel of Fig. 4, showing identical exponential decays with an effective homogeneous linewidth of $\Gamma_{\text{eff}} = 44$ kHz for all three positions across the absorption line. Measured t_{23} decay curves at a fixed t_{12} delay of 200 ns are plotted in the bottom panel of Fig. 4, showing nearly identical behavior. The nonexponential decays reveal the presence of spectral diffusion, and the solid lines are fits of the spectral diffusion model that will be discussed in later sections. The slight differences between the decay curves are most likely due to small changes in sample temperature of much less than 0.1 K between each data set. Together, the results presented in Figs. 3 and 4 confirm that there are no significant variations in the material properties from the center of the absorption line to well out into the tails, indicating that the entire material bandwidth may be employed for optical applications with no variation in performance.

V. SPECTRAL HOLE BURNING

To study the excited-state relaxation, we employed the frequency selective optical saturation recovery method of time-resolved spectral hole burning. Example hole spectra are plotted in the top panel of Fig. 5 at 2.0 K for applied magnetic fields of 1.0 and 2.5 T with $B \parallel \mathbf{D}_1$. In the Er^{3+}-doped Y_2SiO_5 materials, the superhyperfine interaction between the ^{89}Y nuclear spins in the host crystal and the optically active Er^{3+} ions results in a weak distortion of the spectral hole shapes that appears as small side holes or sidebands. Examples of nuclear "spin-flip sidebands" are visible in the top panel of Fig. 5. The frequency shift of the sidebands was characterized as a function of magnetic field strength, with the results plotted in the bottom panel of Fig. 5. From these measurements, we found that the frequency shift of the sidebands relative to the main hole increases linearly with magnetic field strength at 1.90 MHz/T, a relatively small chemical shift from the ^{89}Y free-nucleus gyromagnetic ratio of 2.09 MHz/T. Consequently, we can identify these sidebands as resulting from the small probability for absorption of a photon to drive a nuclear spin flip of a neighboring ^{89}Y, resulting in excitation of Er^{3+} ions shifted from the laser frequency by the spin-flip transition frequency of the ^{89}Y coupled to the Er^{3+} excited state. The sidebands each have an integrated area of approximately 1% relative to the main spectral hole area over the range of magnetic field strengths studied, indicating a total

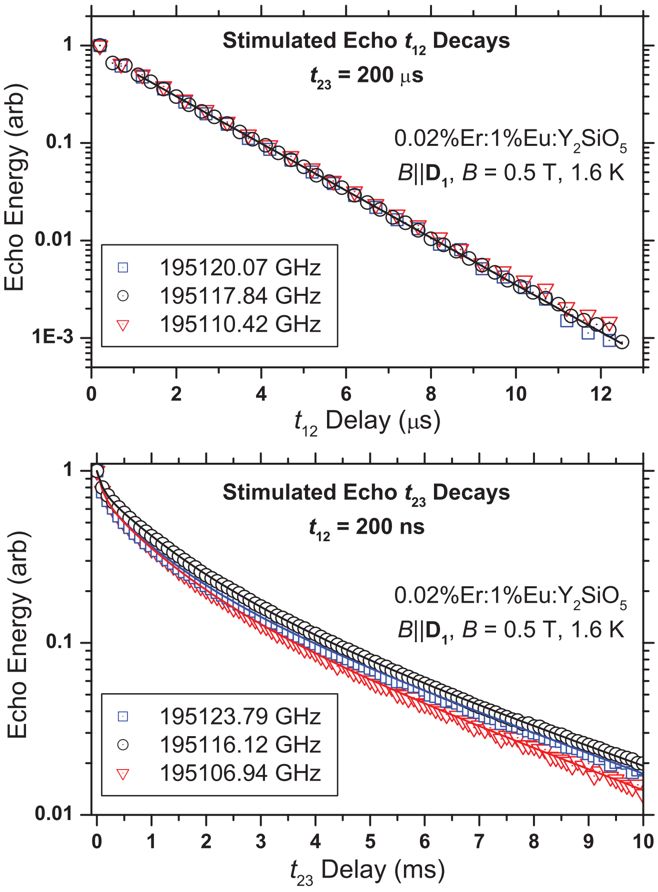

FIG. 4. (Color online) Stimulated echo decays with t_{23} held fixed at 200 μs (top) and with t_{12} held fixed at 200 ns (bottom) measured at different frequencies across the inhomogeneous line. Measured photon echo energies are indicated by symbols and the solid lines are fits of the spectral diffusion model.

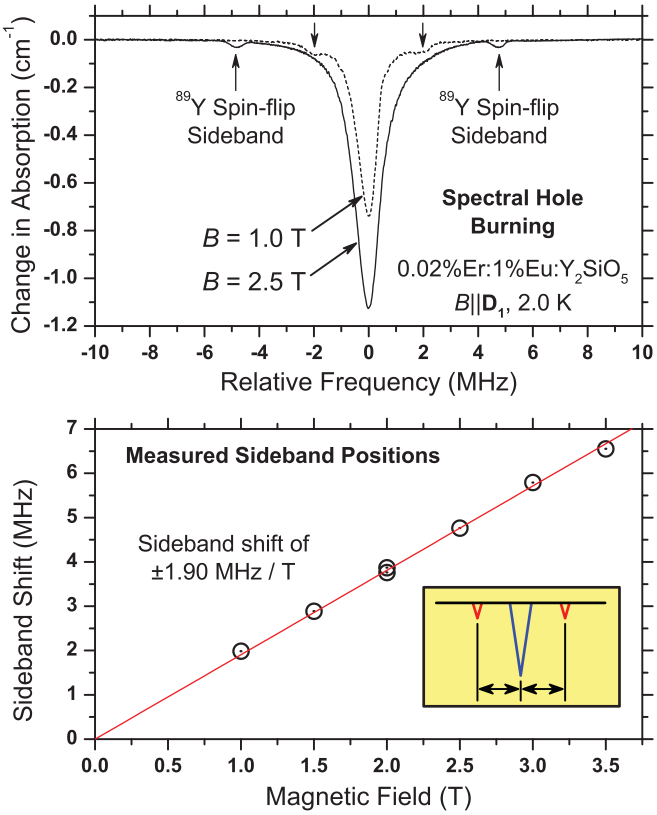

FIG. 5. (Color online) Top: Example hole spectra measured at magnetic fields of 1.0 T (dashed line) and 2.5 T (solid line) showing spin-flip sidebands due to Er^{3+}-^{89}Y superhyperfine coupling. Bottom: Measured frequency shift of the ^{89}Y nuclear spin-flip sidebands as a function of magnetic field strength (circles) revealing a linear shift of 1.90 MHz/T (solid line).

relative transition probability of ∼2% for the Er^{3+} excitation to induce a simultaneous ^{89}Y nuclear spin flip.

We should note that for applications where spectral information is recorded and stored in the optical absorption spectrum, sidebands cause an undesirable distortion of the stored information. For those applications, it may be desirable to operate at low magnetic field strengths where the frequency shift of the sidebands is small enough that they merge into the Lorentzian tails of the main spectral hole. Similar considerations also apply for time-domain optical signal processing applications since the spectral sidebands can produce significant time-dependent modulations of stored coherence, as will be discussed in later sections.

Much weaker and broader spectral sidebands at frequency offsets of ∼850 and ∼750 MHz relative to the main hole were also observed. The frequencies of these sidebands were independent of magnetic field strength, indicating that they likely arise from the hyperfine interaction with the nuclear quadrupole states of the minority ^{167}Er atomic isotope that has a natural abundance of 23% relative to the other Er isotopes. For ^{167}Er, the hyperfine interaction between the $I = 7/2$ nucleus and the electronic doublets can cause each energy level to split into as many as 16 nondegenerate first-order hyperfine levels,[17] resulting in as many as 256 possible optical transitions, many of which may be allowed for some field orientations. For applications such as spectrum analysis, it may be desirable to grow materials doped with an isotope that does not have nuclear spin, such as ^{166}Er, ^{168}Er, or ^{170}Er, to eliminate these additional sideband features. In contrast, applications such as quantum memory may exploit the hyperfine structure to obtain long-lived coherent information storage,[17] requiring samples with enriched levels of ^{167}Er.

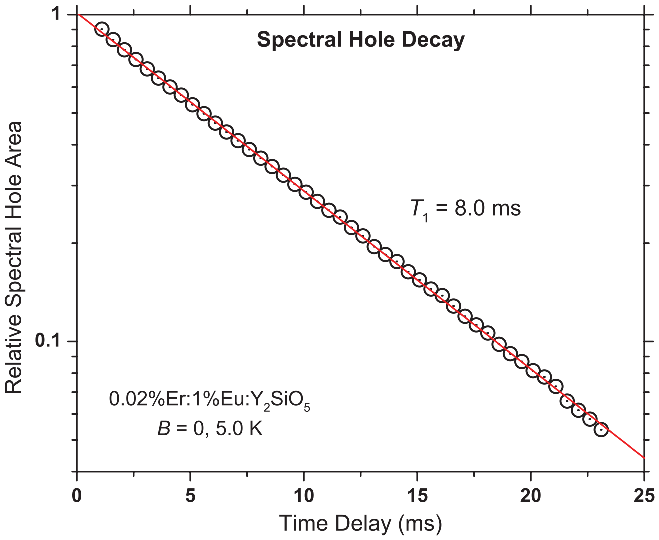

FIG. 6. (Color online) Spectral hole decay measurements (circles) and exponential fit (solid line), revealing an excited-state lifetime of 8.0 ms.

To probe the population relaxation dynamics, we also monitored the decay of the spectral hole area as a function of time delay. Time-resolved hole burning provides a particularly accurate measurement of the excited-state lifetime since the spectral and spatial selectivity of the method circumvents problems such as reabsorption and reemission (radiation trapping)[36] that are often encountered in direct fluorescence decay measurements. These measurements were performed by generating a shallow spectral hole (∼15% increase in transmission) using a 50-μs-long optical pulse, and then probing the spectral hole after a fixed time delay using a 50-μs-long frequency chirped pulse; this sequence was then repeated as a function of readout delay. The time-resolved spectral hole decay measurements are plotted in Fig. 6, displaying an exponential decay with a lifetime of 8.0 ms, corresponding to the $^4I_{13/2}$ excited-state T_1 lifetime. This value is slightly shorter than the previously reported value of 11 ms for $Er:Y_2SiO_5$.[4] Further study is required to determine if this small difference is due to radiation trapping in the fluorescence decay measurements or a real difference in the properties of the two materials.

In addition to measuring the decay of spectral hole area, we also monitored the spectral broadening of the holes as a function of time. We found that the holes broadened to a maximum full-width at half-maximum 5.6 MHz within 100 μs at 5.0 K and weak magnetic fields of ∼0.01 T. This provides an upper estimate for the maximum spectral diffusion broadening for this material, agreeing well with values of 4–5 MHz extracted from the analysis of photon echo decays at low temperature and high applied magnetic field strengths.[22]

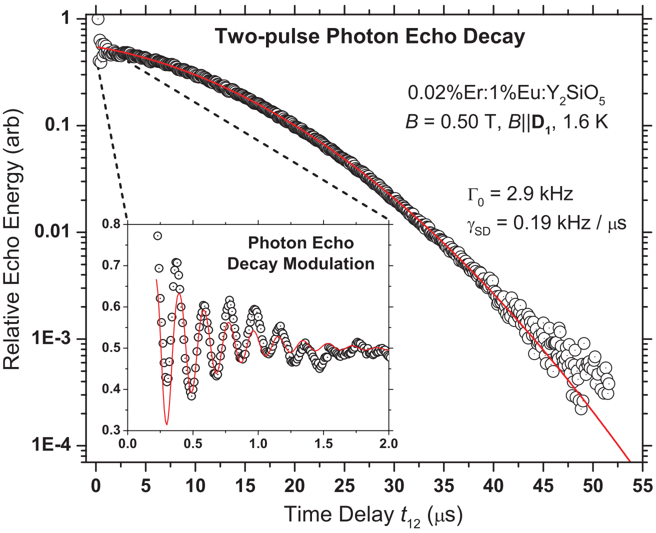

FIG. 7. (Color online) Measured two-pulse photon echo decay curve (circles) with modulation (shown in inset) due to coupling of Er^{3+} to nuclear spins and a nonexponential decay shape indicating excess decoherence caused by spectral diffusion and solid lines are fits of the photon echo decay model.

VI. OPTICAL DECOHERENCE AND SPECTRAL DIFFUSION

To probe the coherence properties of 0.02%Er:1%Eu:Y_2SiO_5, photon echo decay measurements were performed over a wide range of conditions. In solid-state materials, decoherence of optical transitions at low temperatures (<5 K) is often limited by time-dependent perturbations caused by fluctuations in the optical center's local environment. The resulting evolution in decoherence rate and spectral broadening caused by these dynamic perturbations is known as spectral diffusion.[37–41] In particular, spectral diffusion due to magnetic spin-spin interactions between each optically active ion and the other electronic and nuclear spins in the host can be the dominant source of decoherence and spectral broadening for paramagnetic centers such as Er^{3+}. This is demonstrated by the two-pulse photon echo decay presented in Fig. 7, where the nonexponential shape of the echo decay curve results from a progressive increase in the rate of phase decoherence over time that is caused by spectral diffusion. For 0.02%Er:1%Eu:Y_2SiO_5, analysis of photon echo measurements at high magnetic field strengths and low temperatures has demonstrated that the leading source of spectral diffusion in this material under most conditions is magnetic dipole-dipole interactions between the Er^{3+} dopant ions.[22] By studying spectral diffusion in these materials, fundamental insight and practical information are obtained concerning the optical properties of the active ions and the dynamic interactions within the host material.

In addition to the nonexponential decay shape, we also observed significant modulations of the emitted echo energy at short time scales as shown in the panel inset of Fig. 7. This modulation results from coupling to nuclear spins and is the time-domain analog of the spin-flip sideband effect observed in the frequency domain spectral hole-burning measurements described in the previous section. Due to coupling between the electronic and nuclear spins, the simultaneous optical excitation of transitions involving different nuclear spin states results in a quantum interference effect that modulates the stored coherence.[41–45] These modulations of the coherence decay can occur at frequencies corresponding to nuclear spin-state splittings for either the ground or excited electronic states as well as the sums and differences of these frequencies.[41] For the modulation in Fig. 7, we found that the observed modulation frequency of ∼5 MHz did not vary with applied magnetic field strength over the range of conditions studied, indicating that it likely arises from hyperfine coupling to the nuclear quadrupole states of the minority ^{167}Er atomic isotope. In addition to the ∼5-MHz modulation, there is a ∼1-MHz modulation component that does change with magnetic field strength and corresponds to the Er^{3+} superhyperfine coupling with ^{89}Y observed in Fig. 5.

Stimulated photon echo measurements offer one of the most powerful techniques for probing decoherence and spectral diffusion over a wide range of measurement time scales to explore the underlying material physics.[3,46] The time dependence of the stimulated echo intensity depends on both the decoherence and population relaxation dynamics and can be described by

$$I(t_{12},t_{23}) = I_0 e^{\frac{-2t_{23}}{T_1}} e^{-4\pi\Gamma_{\mathrm{eff}} t_{12}} \tag{2}$$

for excitation of a two-level system with an excited-state lifetime of T_1 and a homogeneous ensemble linewidth of Γ_{eff}, where t_{12} is the separation between the first two pulses of the echo sequence and t_{23} is the separation between the second and third pulses of the sequence, sometimes referred to as the waiting time.[3] In the absence of spectral diffusion, Γ_{eff} is a constant equal to the true single-ion homogeneous linewidth Γ_{h} and is related to the phase coherence lifetime T_2 through the relation $\Gamma_{\mathrm{h}} = 1/\pi T_2$.[32] When spectral diffusion is present, we may apply Eq. (2) to describe the stimulated echo behavior by incorporating a time-dependent spectral broadening into Γ_{eff}.[3,46] In this case, Γ_{eff} will depend on both t_{12} and t_{23} as well as the details of the spectral diffusion mechanism and statistics.

When knowledge regarding the spectral diffusion mechanism is available, it can be possible to derive the functional form of Γ_{eff}. For spectral diffusion caused by dilute perturbers in solids, such as the magnetic dipole-dipole interactions between Er^{3+}-dopant ions in Y_2SiO_5, Lorentzian diffusion theory may be applied to describe the behavior using the "sudden jump" model.[38–41] For the conditions studied in this work, we must include spectral diffusion due to magnetic dipole interactions with other Er^{3+} ions residing at both sites 1 and 2, with a different perturbation strength and rate for each site. In this case, we find that Γ_{eff} is approximately described by

$$\Gamma_{\mathrm{eff}}(t_{12},t_{23}) = \Gamma_0 + \sum_i \tfrac{1}{2}\Gamma_i\left[R_i t_{12} + 1 - e^{-R_i t_{23}}\right], \tag{3}$$

where Γ_0 is the linewidth at $t_{12} = t_{23} = 0$ and corresponds to the single-ion linewidth in the absence of spectral diffusion, Γ_1 (Γ_2) is the FWHM magnitude of the distribution of dynamic frequency shifts caused by spectral diffusion from other Er^{3+} ions residing at site 1 (site 2), R_1 (R_2) is the characteristic rate of the spectral diffusion caused by site 1 (site 2) Er^{3+} ions, and the summation is over the two Er^{3+} sites $i = 1,2$.

Examples of fitting Eq. (2) with Γ_{eff} described by Eq. (3) to stimulated photon echo t_{12} and t_{23} decays are shown in Fig. 4 as the solid lines. Fitting to a two-pulse echo decay ($t_{23} = 0$) is shown in Fig. 7, demonstrating the excellent agreement between the model and data. From the fit of the t_{23} decays shown in the bottom panel of Fig. 4, we obtain an estimate of 8 ms for T_1, agreeing with the value of 8.0 ms determined from the spectral hole-burning measurements presented in Fig. 6.

To quantitatively characterize the evolution in decoherence and Γ_{eff} due to spectral diffusion, we have adopted the approach of fitting the measured photon echo decays using Eqs. (2) and (3) and then extrapolating the linewidth to the limit $t_{12} \to 0$ to isolate the spectral diffusion that occurs during the waiting time t_{23}. In this limit, the evolution of the linewidth is simply described by

$$\Gamma_{\mathrm{eff}}(t) = \Gamma_0 + \sum_i \tfrac{1}{2}\Gamma_i[1 - e^{-R_i t}]. \tag{4}$$

This analysis approach is essential for extracting fundamental material properties that accurately describe the behavior of the system for different conditions since both the measurement approach and time scale strongly affect the details of the observed decoherence whenever spectral diffusion is present. For example, the effective linewidth defined by Eq. (4) may be directly related to time-resolved spectral hole-burning results. In that case, a spectral hole measured after a time delay of t will have a Lorentzian line shape with a full-width at half-maximum equal to $2\Gamma_{\mathrm{eff}}$, independent of the relative magnitudes of Γ_0, Γ_1, and Γ_2, providing a convenient correspondence with the traditional result in the absence of spectral diffusion. We have also previously shown how the material's phase memory or coherence lifetime T_M may be calculated from the spectral diffusion parameters extracted from this analysis.[3,46] The T_M value may also be directly determined empirically from any measured Γ_{eff} by simply identifying the point on the time-dependent $\Gamma_{\mathrm{eff}}(t)$ curve where the relation $T_M = 1/\pi\Gamma_{\mathrm{eff}}(T_M)$ is satisfied.[47]

When analyzing photon echo decays, the presence of modulations due to hyperfine or superhyperfine levels can complicate the analysis and potentially introduce errors in the results. For the stimulated photon echo measurements, we found that the superhyperfine coupling to ^{89}Y was the only source of modulation that significantly affected the measured decay curves. While the 5-MHz hyperfine modulation was significant for two-pulse photon echo measurements such as shown in Fig. 7, it generally did not appear in the stimulated echo measurements. The observed ^{89}Y modulations were relatively weak and damped out quickly so that they only have a significant effect on the echo decays at the lowest fields or at high temperatures where the effective linewidth becomes comparable to the modulation frequency. For these cases, extra care is required when analyzing decay curves to distinguish between trends due to a partial period of an echo modulation and the true overall decay trend due to decoherence.

The approach for analyzing echo decays under conditions where echo modulations become problematic is illustrated in Fig. 8 for an applied magnetic field of 0.01 T along the $\mathbf{D}_1$ axis at 1.6 K. A series of stimulated echo t_{12} decays are shown for different values t_{23}, demonstrating how the echo modulations significantly distort the decays for the shorter values of t_{23}. The solid lines plotted in Fig. 8 are fits of the stimulated echo modulation theory including superhyperfine coupling to the ^{89}Y spin-$\frac{1}{2}$ nuclei.[43,44] The fits give excellent agreement with the data over all measured time scales, allowing us to extract the underlying effective homogeneous linewidths. In addition, these fits indicate that there is a local magnetic field of ~0.13 T at the neighboring ^{89}Y nuclei due to the Er^{3+} ion for this external field orientation. This is consistent with extensive electron spin-echo envelope modulation (ESEEM) studies of the Er^{3+}-^{89}Y interaction for the Er^{3+} ground state in this material.[48] The data also reveal that the probability for driving a ^{89}Y nuclear spin flip during optical excitation is ~5% at this low applied magnetic field strength, comparable to the value of ~2% at magnetic fields larger than 1 T that was determined from the spin-flip sideband measurements shown in Fig. 5.

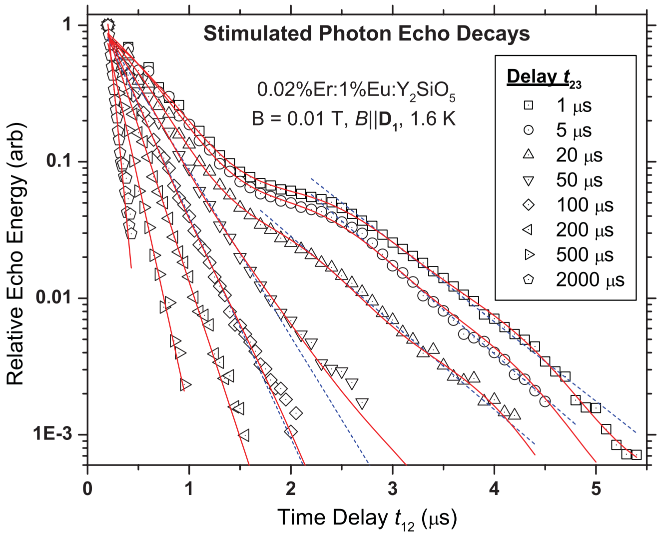

FIG. 8. (Color online) Stimulated photon echo decays for a low magnetic field strength of 0.01 T demonstrating the effect of modulations due to coupling of Er^{3+} to ^{89}Y. Symbols are measured photon echo energies, solid lines are decay fit curves including the superhyperfine interaction, and dashed lines are exponential decays fit to selected portions of the decays.

While fitting the full echo modulation theory gives the most accurate estimates for Γ_{eff} and can reveal important information about the superhyperfine interaction, often it is desirable to apply a less complex approach. For the ^{89}Y modulations, we have found that fitting simple exponential decays to selected regions of the modulation generally gives estimates for Γ_{eff} that are within ±20% of the more accurate value determined from the full modulation theory, an acceptable accuracy comparable to the other experimental errors. Examples of this approach are shown as the dashed lines in Fig. 8, demonstrating this alternative method.

To fully explore the time evolution of the optical decoherence and the corresponding time-dependent increase in Γ_{eff}, we performed stimulated echo t_{12} decay measurements over several orders of magnitude of t_{23} delay times. The large effect of applied magnetic field strength on the decoherence

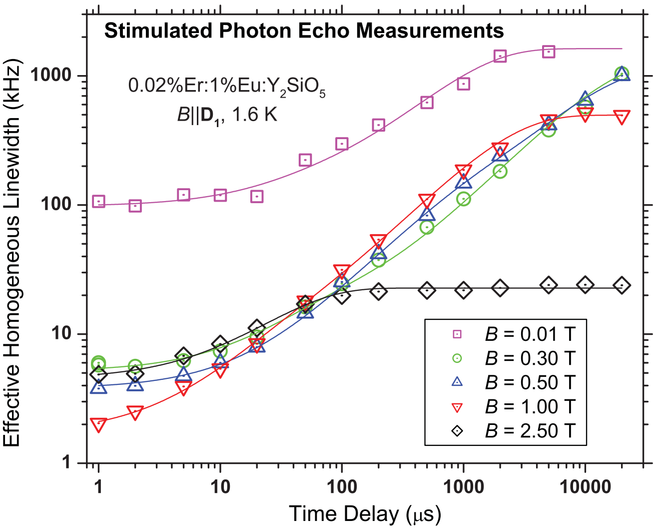

FIG. 9. (Color online) Measured time evolution of the effective homogeneous linewidth (symbols) for different magnetic field strengths applied along the $\mathbf{D}_1$ axis at 1.6 K; solid lines are fits of Eq. (4) for each data set.

evolution is demonstrated in Fig. 9. For these measurements, the time dependence of Γ_{eff} described by (4) was measured at 1.6 K over time scales from 1 μs to 20 ms at different magnetic field strengths from 0.01 to 2.5 T applied along the crystal's $\mathbf{D}_1$ axis. Solid lines are fits of the spectral diffusion model described by Eq. (4), giving excellent agreement. The data show that increasing the magnetic field strength can dramatically suppress the spectral diffusion broadening that occurs, although there can actually be a slight increase in broadening at short time scales as the magnetic field is increased. For example, if we compare measurements at 0.3 and 1.0 T, we observe that the 1.0-T linewidths are narrower for time scales of <50 μs, become broader than the 0.3-T linewidths for time scales from 50 to 500 μs, and then become narrower again at >500 μs. This behavior results from the magnetic field acting to reduce the overall magnitude of the spectral diffusion while simultaneously increasing the spectral diffusion rate so that a larger portion of the broadening occurs at shorter time scales.[46]

As demonstrated by Fig. 9, the applied magnetic field strength has a large effect on the spectral diffusion dynamics. To study this in more detail, we measured Γ_{eff} as a function of magnetic field strength for several values of t_{23}, as shown in the top panel of Fig. 10. The minimum magnetic field strength for these measurements was $\sim$0.005 T, limited by the residual field in the superconducting magnet. The field-dependent shifts of the optical transition frequency were determined by tuning the laser frequency to maximize the photon echo signal at each field. The observed transition frequencies are plotted in the bottom panel of Fig. 10 and indicate a linear shift of +6.5 GHz/T with field. This agrees well with the value of +6.3 GHz/T calculated from the measured ground- and excited-state magnetic g tensors for the b-line transition with this field orientation.[26]

The results presented in Fig. 10 reveal the presence of local maxima and minima in the magnetic field dependence of Γ_{eff}. If we examine the data for a 200-μs delay, for example, Γ_{eff} rapidly decreases as the magnetic field is increased, reaching a local minimum of 39 kHz at 0.3 T, then increases again to a local maximum of 73 kHz at 1.6 T, and then decreases monotonically for higher fields. As the magnetic field is increased, the rate of electron spin flips increases due to the strong magnetic field dependence of the direct phonon relaxation mechanism while the overall magnitude of the magnetic disorder decreases due to the increased spin alignment enforced by the field.[41] These characteristic aspects of the spin dynamics allow us to identify Er^{3+} electron spin flips as the source of the spectral diffusion.[3] The different effects of magnetic field strength on the spectral diffusion rate and magnitude predict local minima in the decoherence rate under some conditions,[46] as observed in Fig. 10.

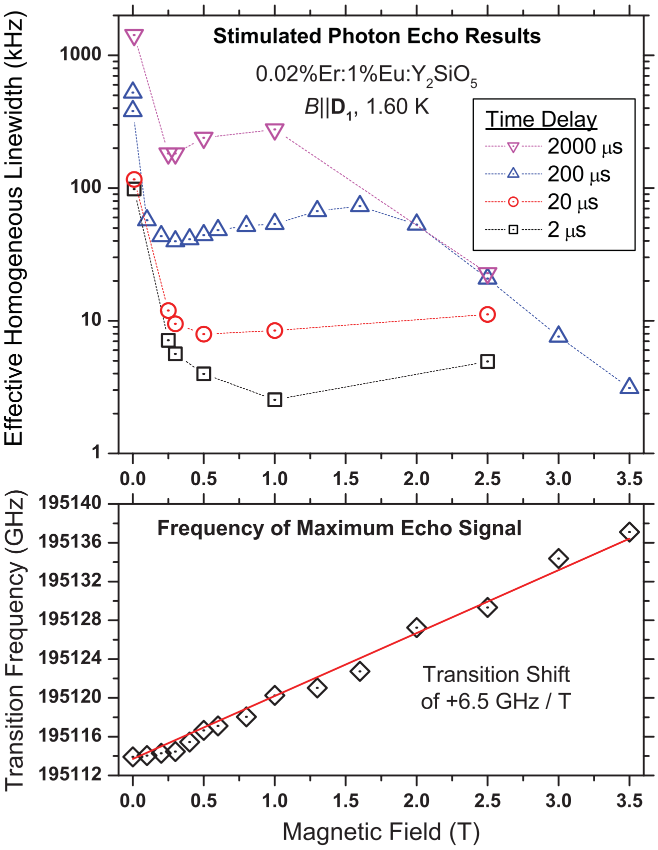

FIG. 10. (Color online) Top: Variation of effective homogeneous linewidth with applied magnetic field strength for different readout delays at 1.6 K for B applied along the $\mathbf{D}_1$ axis. Bottom: Transition frequencies determined by maximizing the photon echo signal at each field (symbols) revealing a linear shift of +6.5 GHz/T (solid line).

While we have successfully applied the spectral diffusion model to quantitatively describe and predict the variations in the magnetic field dependence of Γ_{eff} with time scale, temperature, and concentration for $\mathrm{Er{:}LiNbO_3}$,[46] this is more difficult for Er^{3+} in $\mathrm{Y_2SiO_5}$ due to contributions from two different Er^{3+} sites, each with different coupling strengths and spin dynamics, and the nonlinear Zeeman effect observed for some of the electronic states involved. Nevertheless, we may qualitatively analyze the observed behavior to understand the dominant spectral diffusion mechanisms acting at different magnetic field strengths. For the conditions in Fig. 10, at fields between ∼0.1 and ∼0.5 T, the spectral diffusion is driven by Er^{3+} spin flip-flops. For fields between ∼0.5 and ∼1.0 T, the spectral diffusion arises from phonon-driven spin flips of Er^{3+} ions at site 2 with a smaller contribution from Er^{3+} ions at site 1. For fields between ∼1 and ∼5 T, the spectral diffusion is dominated by phonon-driven spin flips of Er^{3+} ions at site 1. For different temperatures, Er^{3+} doping concentrations, and magnetic field orientations, the relative importance of each spectral diffusion component will vary; however, the general behavior may still be understood within this picture for the spectral diffusion dynamics.

It is well known that the large magnetic anisotropy of the Er^{3+} ions in Y_2SiO_5 causes the material properties to depend strongly on the precise orientation of the externally applied magnetic field.[5,17,26] Orientation-dependent two-pulse photon echo measurements on 0.0015%Er:Y_2SiO_5 at field strengths above 1 T have been previously reported;[5] however, no information is available for lower field strengths and higher Er^{3+} concentrations or for how the field orientation affects the time-dependent evolution of the decoherence. Consequently, we studied the orientation dependence of the effective homogeneous linewidth for a full 360° rotation of the magnetic field within the $\mathbf{D}_1$-$\mathbf{D}_2$ plane. Furthermore, we examined the dependence over three orders of magnitude of t_{23} delay to determine the effect of spectral diffusion. For these measurements, we chose to study the 0.02%Er:Y_2SiO_5 crystal so that we could selectively probe only the *b*-line transition for all magnetic field orientations. While we do expect some difference in the decoherence properties of the Eu-doped material, these measurements provide an overview of the spectral diffusion behavior with field orientation and avoid complications arising from the varying overlap and relative amplitude of the *b*-line and *c*-line transitions that occur for the Eu-doped material as the field orientation is rotated.

The measured magnetic field orientation dependence of the effective homogeneous linewidth for t_{23} delays from 2 μs to 2 ms is shown in the top panel of Fig. 11 for a field strength of 0.5 T at 1.6 K, demonstrating the complex variation in Γ_{eff} with field orientation and measurement time scale. The bottom panel of Fig. 11 gives the corresponding measured optical transition frequency at each orientation; we expect the corresponding transition frequencies in the 1%Eu-doped material to be shifted lower by 3 GHz relative to these values in Er:Y_2SiO_5, as observed in Fig. 2. From the results in Fig. 11, we see that spectral diffusion is suppressed for orientations of 40° to 20° between the $\mathbf{D}_1$ and $\mathbf{D}_2$ directions, depending on the measurement time scale. These orientations are nearly parallel to the crystal's **c** axis, providing a convenient method for identifying the optimum field orientation for an x-ray-oriented sample. At the optimum orientations, the effective linewidth is decreased by a factor of 2 to 5 at different delays compared to the values with $B \| \mathbf{D}_1$ for these conditions. By comparing the effective linewidths at different time scales, we observed that the magnetic field orientation influences the decoherence through both the magnitude and rate of the spectral diffusion processes. The low C_1 point symmetry of the Er^{3+} sites, which leads to different magnetic *g*-tensor orientations for the ground and excited states of each site,[26] combined with the lack of knowledge of the orientation dependence of material properties such as the anisotropic phonon coupling strength, prevents quantitative modeling of the spectral diffusion orientation dependence in Er:Y_2SiO_5, highlighting the need for these types of detailed measurements.

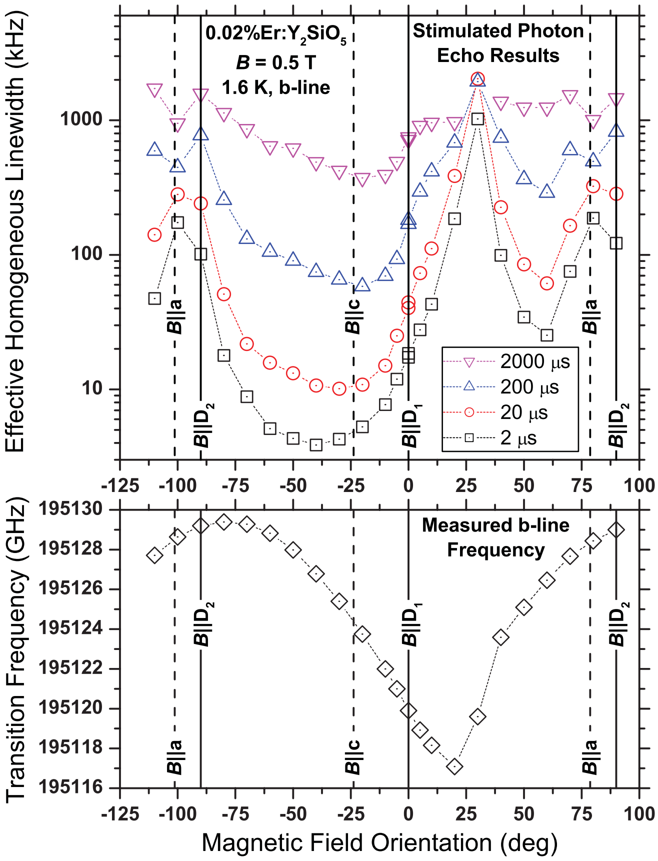

FIG. 11. (Color online) Top: Full orientation dependence of decoherence as a function of readout delay for the *b*-line transition in 0.02%Er:Y_2SiO_5 at $B = 0.5$ T with the applied magnetic field direction in the crystal's $\mathbf{D}_1$-$\mathbf{D}_2$ plane. Bottom: Measured optical transition frequency of *b* line at each orientation. Solid vertical lines mark the orientations of the $\mathbf{D}_1$ and $\mathbf{D}_2$ extinction axes and vertical dashed lines mark the **a** and **c** crystallographic axes.

As discussed previously, the absorption line of 0.02%Er:1%Eu:Y_2SiO_5 is composed of two overlapping transitions that may potentially exhibit different optical decoherence properties. The results presented in Figs. 3 and 4 did not reveal any significant variations in decoherence across the absorption line, suggesting that the properties of the *b*-line and *c*-line transitions are similar for the conditions examined. To further investigate this, we measured the decoherence evolution for these two transitions in the 0.02%Er:Y_2SiO_5 material where they are spectrally resolved and may be individually studied. The measured evolution of the effective linewidth is shown in Fig. 12, where we observe that there is no significant difference in decoherence over all measured time scales under these conditions. The measured values for the *c*-line transition tend to be slightly larger than the *b*-line values, but well within the experimental accuracy of the measurements.

In addition to verifying that the entire transition bandwidth exhibits uniform spectral resolution, this result also indicates that the upper sublevels of both the ground- and excited-state

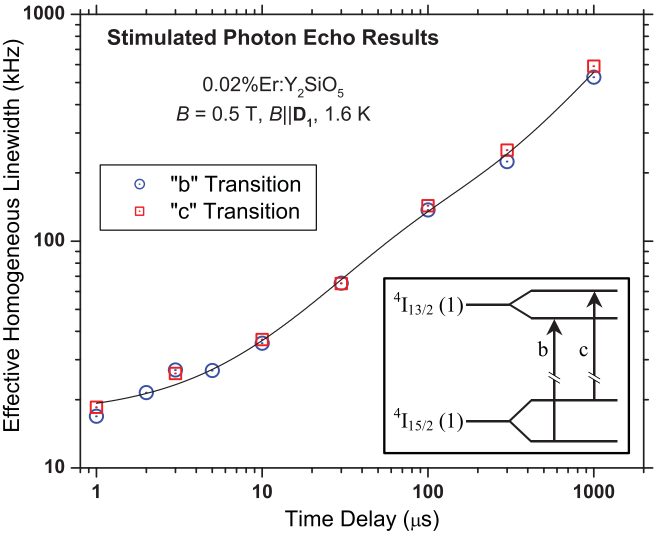

FIG. 12. (Color online) Comparison of measured effective homogeneous linewidths (symbols) over different time scales for the "b" and "c" optical transitions in 0.02%Er:Y$_2$SiO$_5$ at 1.6 K with an applied field of 0.5 T along the $\mathbf{D}_1$ axis. The solid line is a fit of the spectral diffusion model.

doublets relax relatively slowly so that their decoherence is not lifetime limited. This result is significant since it indicates that the upper Zeeman sublevel for either the ground or excited state could be employed in a Λ or V system for quantum information applications[18,19,21] without negative consequences for the decoherence rates.

In addition to studying the effects of applied magnetic fields on Γ_{eff}, the effect of crystal temperature on the time dependence of Γ_{eff} was also studied for different magnetic field strengths. An example of this is shown in Fig. 13, where the measured time evolution of Γ_{eff} at 5.0 K is plotted for applied fields from 0.01 to 3.0 T, and the solid lines are fits of the spectral diffusion model. These results show that Γ_{eff} initially increases as the magnetic field is increased up to 0.5 T, and then rapidly decreases at higher fields.

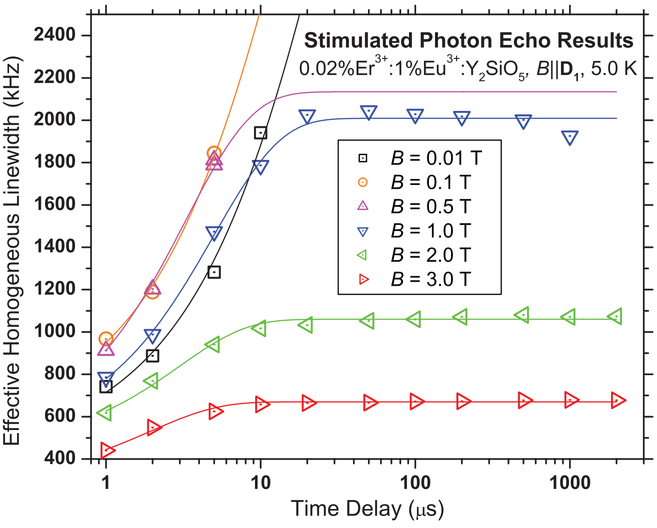

FIG. 13. (Color online) Decoherence evolution at different applied magnetic field strengths for a sample temperature of 5.0 K. Symbols are measured effective homogeneous linewidths and solid lines are fits of the spectral diffusion model described by Eq. (4).

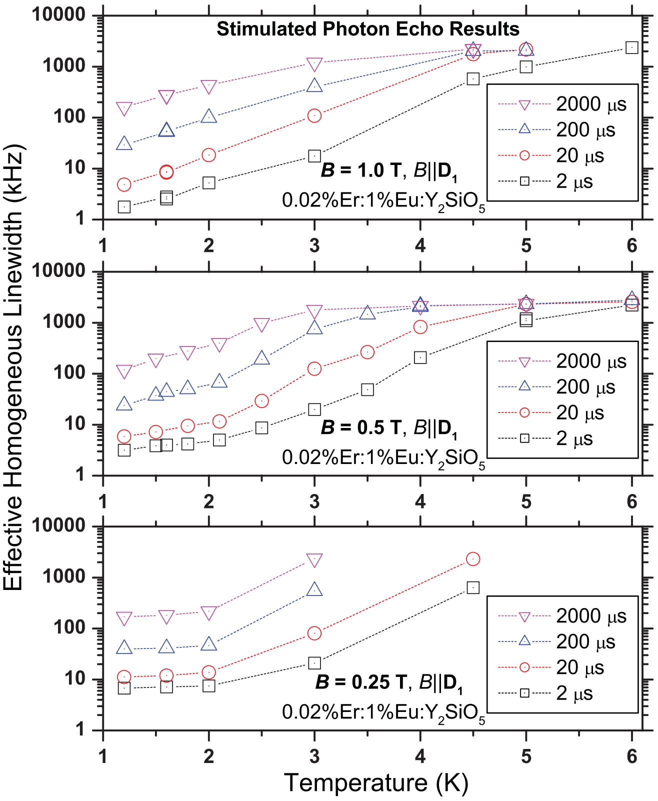

FIG. 14. (Color online) Temperature dependence of effective homogeneous linewidth at different readout delays for applied field strengths of 0.25 T (bottom), 0.5 T (middle), and 1.0 T (top) with $B \| \mathbf{D}_1$.

We also studied the variation in Γ_{eff} with temperature from 1.2 to 6.0 K for time scales of 2 μs, 20 μs, 200 μs, and 2 ms and magnetic field strengths of 0.25, 0.5, and 1.0 T with $B \| \mathbf{D}_1$. The results of these measurements are presented in Fig. 14. These measurements reveal a nearly exponential increase in Γ_{eff} with temperature over all time scales until a maximum value of 2–3 MHz is reached. This value for the saturated spectral diffusion broadening at higher temperatures agrees well with our measured spectral hole widths of $2\Gamma_{\text{eff}} = 5.6$ MHz that gives a maximum value of 2.8 MHz for Γ_{eff}. This is also consistent with the spectral diffusion parameters previously determined at low temperatures and high fields that predict a maximum value of 2.0–2.5 MHz, not including the contribution from spectral diffusion due to site 2 Er^{3+} spins.[22] In addition to the increase in spectral diffusion, we also expect an increase in the single-ion homogeneous linewidth Γ_0 at higher temperatures due to elastic phonon scattering processes,[49] although that is only expected to become significant for temperatures above ~5 K.

While analyzing the nonexponential photon echo decay curves allows Γ_{eff} to be unambiguously determined, the shape of the decay curves also contains information about the instantaneous rate of broadening caused by spectral diffusion.[46] If we consider a single homogeneous ensemble of ions in the material, the spectral width of the ensemble will initially broaden linearly with time due to spectral diffusion,

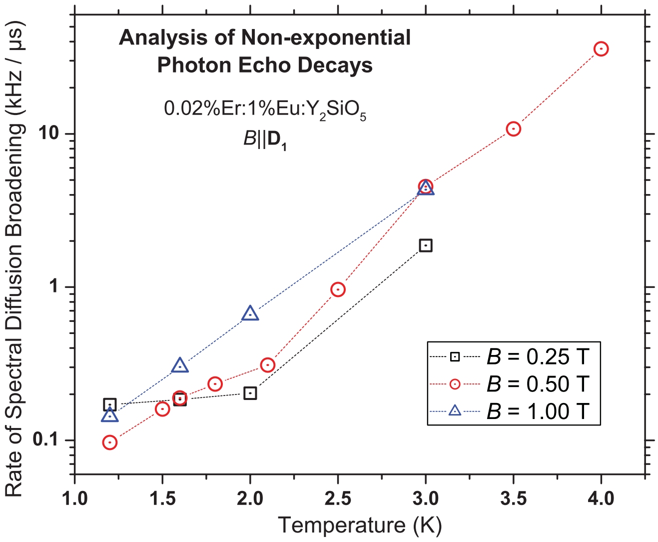

FIG. 15. (Color online) Rate of spectral diffusion broadening extracted from analysis of nonexponential photon echo decays at different temperatures and magnetic field strengths.

until the time scale begins to approach either $1/R_1$ or $1/R_2$. Using Eq. (4) in the limits of $t \ll 1/R_1$ and $t \ll 1/R_2$, over a time of Δt the linewidth increase an amount $\Delta\Gamma_{\text{eff}}$ given by the approximate relation

$$\Delta\Gamma_{\text{eff}} \sim \tfrac{1}{2}\left(\Gamma_1 R_1 + \Gamma_2 R_2\right)\Delta t = \gamma_{\text{SD}}\Delta t, \qquad (5)$$

where γ_{SD} is the instantaneous rate of spectral diffusion broadening. By fitting Eqs. (2) and (3) to the observed echo decays, we can determine γ_{SD} and estimate how quickly a spectral feature stored in the material will broaden with time. The results of this analysis are plotted in Fig. 15 for the 2-μs time scale data of Fig. 14. From these results, we see that the rate of spectral diffusion broadening increases exponentially with temperature from $\sim$0.1 kHz/μs at 1.2 K to $\sim$40 kHz/μs at 4.0 K. We also observe that the data at the smallest magnetic field strength has the fastest rate of broadening at low temperatures, while it has the slowest rate of broadening at higher temperatures. In addition to providing more insight into the spectral diffusion dynamics, this analysis is also more broadly useful by providing a simple and practical metric for understanding how quickly information stored in the material is lost due to spectral diffusion.

VII. EFFECT OF STATIC DISORDER ON DECOHERENCE DYNAMICS

It has been previously reported that codoping with Eu^{3+} has no effect on the optical decoherence properties of Er^{3+} in Y$_2$SiO$_5$ at low temperature (1.6 K) and high magnetic field strengths (>1 T).[22] To determine if there are differences in the properties of the materials at low magnetic field strengths (<1 T), we performed stimulated echo measurements at 1.6 K for 0.5 T with $B \| \mathbf{D}_1$ on both 0.02%Er:1%Eu:Y$_2$SiO$_5$ and 0.02%Er:Y$_2$SiO$_5$ to compare the time-dependent decoherence of the materials. The results of these measurements are presented in Fig. 16, revealing that the Eu^{3+}-doped material exhibits significantly less decoherence over all time scales from 1 μs to 1 ms for these conditions. As the field strength is further reduced, we found that the difference between the materials becomes even more pronounced, allowing relatively modest decoherence rates to be observed even at very low magnetic field strengths of <0.01 T in the 0.02%Er:1%Eu:Y$_2$SiO$_5$ sample. To verify that this effect is not a result of different Er^{3+} ion densities, we compared the integrated absorption line strengths measured from laser absorption spectra of both Er^{3+} sites for these two samples and determined that the Er^{3+} concentrations are the same in both materials to within ±10%. These observations suggest that the Eu^{3+} doping does inhibit the spectral diffusion dynamics.

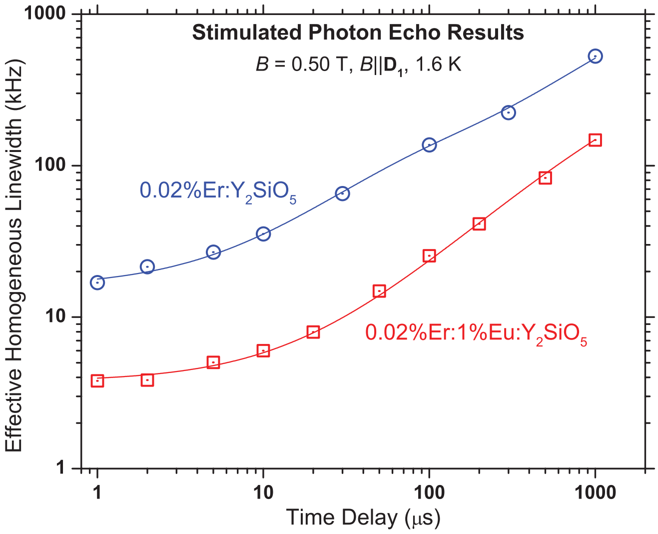

FIG. 16. (Color online) Comparison of decoherence in the 0.02%Er:1%Eu:Y$_2$SiO$_5$ and 0.02%Er:Y$_2$SiO$_5$ materials.

The suppression of decoherence in the Eu-doped material may be understood by considering the influence of the static disorder on the Er^{3+} electron spin-flip dynamics. At high magnetic field strengths (>1 T) and low Er^{3+} concentrations, the dominant source of spectral diffusion is Er^{3+} spin flips driven by direct phonon absorption and emission.[3] We do not expect this process to be affected by the Eu^{3+} doping, in agreement with measurements at high magnetic field strengths.[22] As the magnetic field strength is reduced, the direct phonon relaxation process becomes less significant, while Er^{3+} spin-spin relaxation begins to become a more significant mechanism for driving spectral diffusion, particularly at higher Er^{3+} concentrations.[46] In this process, the transverse components of the Er^{3+} dipole-dipole interaction induce mutual spin "flip-flops" that cause two antiparallel Er^{3+} spins to simultaneously flip.[41,50] Although this mechanism involves correlated spin flips and does not affect the net magnetization of the sample, flip-flops result in electron "spin diffusion" that randomizes the local spin orientations and therefore contributes to spectral diffusion. In fact, because the flip-flop process causes two correlated perturbations in the local spin environment, it tends to produce accelerated decoherence and photon echo decays with a more pronounced nonexponential character.[51,52]

The flip-flop process requires resonant antiparallel spins that are in close proximity to each other; consequently, it is rapidly suppressed at higher magnetic field strengths and lower temperatures due to the increase in overall spin alignment. Furthermore, the pair of Er^{3+} ions must also have the same spin-flip transition frequency for the flip-flop process to conserve energy. Because inhomogeneous broadening of the Er^{3+} paramagnetic resonance linewidth reduces the number of Er^{3+} ions that are resonant with each other, the increase in linewidth due to static lattice strain acts to inhibit the spin flip-flop process. From Eq. (5), we see that the decoherence and spectral broadening due to spin flip-flops is directly proportional to the flip-flop rate. Consequently, we expect that increasing the Eu^{3+} concentration to further increase the inhomogeneous broadening should result in even greater suppression of the decoherence at low fields.

As a test of this interpretation for the difference in the effective homogeneous linewidths, we compared fits of the spectral diffusion model given by Eq. (4) for the two different materials, as shown by the solid lines in Fig. 16. To generate these spectral diffusion curves, only the homogeneous linewidth Γ_0 and the spectral diffusion rates R_1 and R_2 for sites 1 and 2 Er^{3+} perturbing spins were allowed to vary, while the magnitudes of the Er^{3+}-Er^{3+} interactions with both sites, described by Γ_1 and Γ_2, were kept constant. For the 0.02%$Er{:}Y_2SiO_5$ data, fitting the Er^{3+}-Er^{3+} spectral diffusion model gave values of $\Gamma_0 = 15.7$ kHz, $\Gamma_1 = 2200$ kHz, $R_1 = 0.49$ kHz, $\Gamma_2 = 160$ kHz, $R_2 = 20$ kHz for these conditions. For the 0.02%Er:1%$Eu{:}Y_2SiO_5$ data, the model gives excellent agreement with the observed data by just reducing the rates to $R_1 = 0.08$ kHz, $R_2 = 1.6$ kHz, and the homogeneous linewidth to $\Gamma_0 = 3.7$ kHz, corresponding to the curve shown in Fig. 16. Since we expect the change in sites 1 and 2 flip-flop rates to be inversely proportional to the electron paramagnetic resonance (EPR) linewidths for the two sites,[41] measuring the change in EPR linewidths and spectral diffusion rates with Eu^{3+} doping would be a conclusive test of this model.

It is important to note that some suppression of nuclear spin flip-flops in the Eu^{3+}-doped material should be expected due to the increased disorder. Consequently, a reduction in spectral diffusion from ^{89}Y spins in the bulk of the crystal may contribute to the decrease of Γ_0 in the Eu^{3+}-doped sample. As a result, introducing disorder into a material may allow us to more closely approach the fundamental quantum limit of decoherence since nuclear spin flip-flops are often the leading source of excess decoherence at high magnetic field strengths and low temperatures.

VIII. ION-ION COUPLING AND INSTANTANEOUS SPECTRAL DIFFUSION

The excess spectral broadening that occurs due to optical excitation is another material property that is important for many applications. This excitation-induced spectral broadening, or “instantaneous spectral diffusion” (ISD), is caused by changes in the ion-ion interactions as random distributions of Er^{3+} in the material are excited into a different electronic state.[38,53–56] As a result, the ISD process in a material must be studied to predict how changes in overall optical excitation density affect the material’s decoherence rate and spectral resolution. It is also important to understand ISD in a material to characterize ion-ion coupling that may be exploited in quantum information applications to enable entanglement between qubits.

For paramagnetic Er^{3+} materials, ISD is usually dominated by magnetic dipole-dipole interactions between the Er^{3+} ions.[53,55] Electric dipole-dipole interactions tend to be more important for diamagnetic systems,[56] although they can also contribute to Er^{3+} ISD. When an Er^{3+} ion is optically excited, the change in magnetic moment between the ground and excited electronic states causes a change in the ion’s magnetic field, perturbing all the other Er^{3+} in the environment. Consequently, as the number of excited Er^{3+} ions increases, ISD produces an increase in the effective homogeneous linewidth of Γ_{ISD} that is described by

$$\Gamma_{\mathrm{ISD}} = \gamma_{\mathrm{ISD}} n_{\mathrm{exc}}, \tag{6}$$

where n_{exc} is the spatial density of excited ions and γ_{ISD} is a coefficient determined by the ion-ion interaction strength.[38,41,55,56]

To study ISD, we employ a stimulated photon echo technique. In this method, a broadband, high-intensity excitation pulse is applied during the t_{23} section of the stimulated echo sequence to produce ISD that is then observed as a change in the magnitude of Γ_{eff} determined from the echo decay curve. The optical frequency of the excitation pulse is shifted so that there is no spectral overlap with the echo pulses to avoid interference between the excitation pulse and the photon echo generation process. In addition, the excitation pulse frequency is chirped over a range of frequencies to excite a wide spectral band of Er^{3+} ions in the absorption line and maximize the excitation density created. Since we expect the Er^{3+} ion-ion interactions and corresponding ISD to be the same in 0.02%$Er{:}Y_2SiO_5$ and 0.02%Er:1%$Eu{:}Y_2SiO_5$, we performed the ISD measurements on the 0.02%$Er{:}Y_2SiO_5$ sample because the much narrower absorption linewidth of 340 MHz allowed us to excite a large fraction of the Er^{3+} ions using a 100-MHz frequency chirp, rather than the multigigahertz frequency chirp that would be required to excite an equivalent number of ions in the Eu-doped material.

Generally, the most difficult aspect of characterizing ISD is accurately determining the actual n_{exc} generated in the volume of the sample probed. While the usual approach is to estimate the intensity profile of the excitation laser spot in the sample and then calculate the expected excited-state population, we employed an alternate method using three independent laser sources for a complete, controlled, and well-calibrated measurement of the ISD. The first laser was used to generate the pulses in the photon echo sequence. The second frequency-chirped laser generated the Er^{3+} excitation at a different frequency in the absorption line. The third laser was attenuated so that it had no effect on the level of excitation and frequency chirped across the region of the absorption spectrum excited by the second laser to directly measure the change in optical absorption due to the excitation pulse. All three lasers were combined in a single-mode optical fiber and launched collinear into the crystal to guarantee perfect spatial overlap of all three beams. This method allowed us to precisely determine the actual amount of optical excitation since the measured absorption coefficient α is directly related to the Er^{3+} excited state population n_{exc} through the relation

$$\alpha = \sigma\,(N - 2n_{\mathrm{exc}})\,, \tag{7}$$

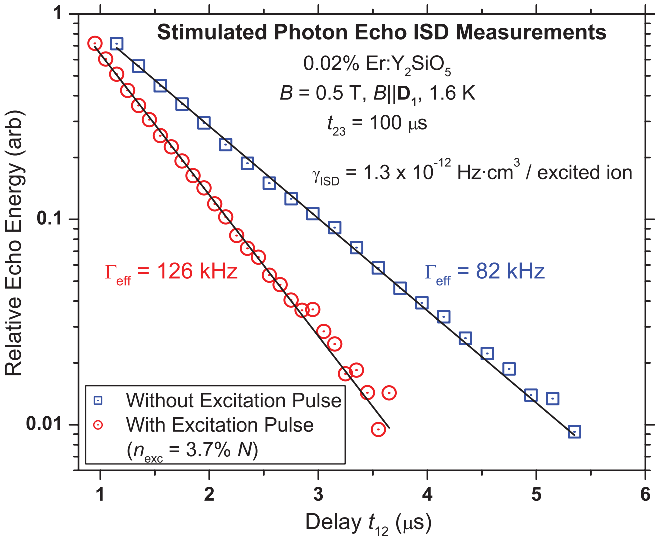

FIG. 17. (Color online) Measurement of increased decoherence due to instantaneous spectral diffusion in 0.02%Er:Y$_2$SiO$_5$.

where σ is the Er^{3+} absorption cross section and N is the total Er^{3+} ion density equal to 1.83×10^{18} ions/cm^3 for each site at a 0.02% Er^{3+} doping level. As a result, we may directly determine n_{exc} by measuring the change in integrated absorption coefficient caused by the excitation pulse using the relation

$$n_{\text{exc}} = \frac{N}{2}\left(1 - \frac{\int \alpha d\nu}{\int \alpha_0 d\nu}\right), \tag{8}$$

where α_0 and α are the measured frequency-dependent absorption coefficients before and after the excitation pulse, respectively, and the integrations are over optical frequency ν. The value of n_{exc} obtained by this method represents an intensity-weighted average excitation level throughout the entire beam path in the sample. Because the photon echo signal is predominately generated in the regions of the sample with the highest levels of excitation, the effective value of n_{exc} in a photon echo measurement may be larger than the value determined using Eq. (8) under some conditions, causing the ISD to be overestimated. To minimize this effect, we used a thin sample that was 1.4 mm thick in our measurements and we used an excitation pulse power sufficient to reduce the residual absorption of the sample to less than 50% so that there was a uniform level of excitation along the beam path.

The results of ISD measurements at 1.6 K are plotted in Fig. 17 for $B = 0.5$ T with $B \| \mathbf{D}_1$. In these measurements, a delay of $t_{23} = 100$ μs was used with an 80-μs-long excitation pulse that was frequency chirped over a 100-MHz bandwidth during the 100-μs delay. We observed Γ_{eff} increase from 82 kHz without the excitation pulse to 126 kHz when the excitation pulse was applied. Since the excitation pulse is applied during the t_{23} section of the echo sequence, it only produces decoherence during the last t_{12} section of the echo generation process. As a result, the actual underlying spectral broadening Γ_{ISD} corresponds to twice the change in effective linewidth Γ_{eff} determined from the echo decay, giving a value of $\Gamma_{\text{ISD}} = 88$ kHz. From the measured change in absorption coefficient and Eq. (8), we found that 3.7% of all Er^{3+} ions at site 1 were excited by the excitation pulse, corresponding to $n_{\text{exc}} = 6.77 \times 10^{16}$ ions/cm^3. Combining these results with Eq. (6) gives an ISD coefficient of $\gamma_{\text{ISD}} = 1.3 \times 10^{-12}$ Hz cm^3/excited ion. For comparison, this value is similar to the value of $\gamma_{\text{ISD}} = 1.2 \times 10^{-12}$ Hz cm^3/excited ion for Tm:YAG at 793 nm,[25] revealing that these materials have similar levels of ISD broadening for the conditions studied.

IX. CONCLUSIONS

With dual goals of characterizing the 0.02%Er:1%Eu:Y$_2$SiO$_5$ material and, more generally, expanding the understanding of spectral diffusion in paramagnetic materials, the dynamic optical properties of 0.02%Er:1%Eu:Y$_2$SiO$_5$ were studied. The experimental results together with detailed analysis provide an overview of the optical decoherence and spectral resolution of the site 1 transition at 1536 nm in 0.02%Er:1%Eu:Y$_2$SiO$_5$ for conditions of temperature and magnetic field strength relevant for operation with closed-cycle cryostats and fields generated by simple permanent magnet arrangements. Decoherence was measured and analyzed for different conditions of applied magnetic field strength, field orientation, temperature, optical frequency, measurement time scale, and excitation density. Hole-burning dynamics and superhyperfine interactions with ^{89}Y were also observed. Information on ion-ion interactions from this study also suggests a possible avenue for using Er^{3+} and Eu^{3+} double doping in quantum information systems, providing long-term memory in the highly isolated nuclear spins of the Eu^{3+} ground state and operation at 1.5 microns using Er^{3+} electronic transitions. All of these measurements are of immediate significance for employing this system in spatial-spectral holography and quantum information science applications.[6–21] Moreover, these results are particularly important for guiding more comprehensive studies of decoherence and spectral resolution throughout the complex multidimensional parameter space spanning time scale, magnetic field strength and orientation, temperature, and crystal composition.

This study also provides insight into how selective introduction of specific chemical impurities into a material can produce controlled disorder in the crystalline environment to modify static properties such as lattice strain as well as dynamic properties such as spin diffusion rates. Continuing to improve our understanding of disorder in crystalline materials is essential for achieving the ultimate goal of engineering the chemical composition of materials to optimize properties such as bandwidth and decoherence for device applications.

ACKNOWLEDGMENTS

The authors wish to thank T. Böttger, Y. Sun, and R. M. Macfarlane for many valuable discussions on spectral diffusion and the optical properties of Er^{3+}-doped Y$_2$SiO$_5$. The results presented here are based on work supported by the Space and Naval Warfare Systems Center Pacific under Contract No. N66001-09-C-2002.

[*] thiel@physics.montana.edu
[†] babbitt@physics.montana.edu
[‡] cone@montana.edu

[1] R. M. Macfarlane, T. L. Harris, Y. Sun, R. L. Cone, and R. W. Equall, Opt. Lett. **22**, 871 (1997).

[2] T. Böttger, Y. Sun, C. W. Thiel, and R. L. Cone, Proc. SPIE **4988**, 51 (2003).

[3] T. Böttger, C. W. Thiel, Y. Sun, and R. L. Cone, Phys. Rev. B **73**, 075101 (2006).

[4] T. Böttger, Y. Sun, C. W. Thiel, and R. L. Cone, Phys. Rev. B **74**, 075107 (2006).

[5] T. Böttger, C. W. Thiel, R. L. Cone, and Y. Sun, Phys. Rev. B **79**, 115104 (2009).

[6] Z. Cole, Thomas Böttger, R. Krishna Mohan, R. Reibel, W. R. Babbitt, R. L. Cone, and K. D. Merkel, Appl. Phys. Lett. **81**, 3525 (2002).

[7] T. L. Harris, Y. Sun, R. L. Cone, W. R. Babbitt, J. A. Ritcey, and R. W. Equall, Opt. Lett. **25**, 85 (2000).

[8] T. L. Harris, Y. Sun, R. L. Cone, R. M. Macfarlane, and R. W. Equall, Opt. Lett. **23**, 636 (1998).

[9] V. Crozatier, G. Gorju, F. Bretenaker, J.-L. Le Gouët, and I. Lorgere, Opt. Lett. **31**, 3264 (2006).

[10] P. B. Sellin, N. M. Strickland, T. Böttger, J. L. Carlsten, and R. L. Cone, Phys. Rev. B **63**, 155111 (2001).

[11] T. Böttger, Y. Sun, G. J. Pryde, G. Reinemer, and R. L. Cone, J. Lumin. **94-95**, 565 (2001).

[12] T. Böttger, G. J. Pryde, N. M. Strickland, P. B. Sellin, and R. L. Cone, Opt. Photonics News **12**, 23 (2001).

[13] E. Baldit, K. Bencheikh, P. Monnier, S. Briaudeau, J. A. Levenson, V. Crozatier, I. Lorgeré, F. Bretenaker, J. L. Le Gouët, O. Guillot-Noël, and Ph. Goldner, Phys. Rev. B **81**, 144303 (2010).

[14] E. Baldit, K. Bencheikh, P. Monnier, J. A. Levenson, and V. Rouget, Phys. Rev. Lett. **95**, 143601 (2005).

[15] B. Lauritzen, J. Minář, H. de Riedmatten, M. Afzelius, N. Sangouard, C. Simon, and N. Gisin, Phys. Rev. Lett. **104**, 080502 (2010).

[16] C. W. Thiel, T. Böttger, and R. L. Cone, J. Lumin. **131**, 353 (2011).

[17] O. Guillot-Noël, Ph. Goldner, Y. Le Du, E. Baldit, P. Monnier, and K. Bencheikh, Phys. Rev. B **74**, 214409 (2006).

[18] S. R. Hastings-Simon, B. Lauritzen, M. U. Staudt, J. L. M. van Mechelen, C. Simon, H. de Riedmatten, M. Afzelius, and N. Gisin, Phys. Rev. B **78**, 085410 (2008).

[19] B. Lauritzen, S. R. Hastings-Simon, H. de Riedmatten, M. Afzelius, and N. Gisin, Phys. Rev. A **78**, 043402 (2008).

[20] W. Tittel, M. Afzelius, R. L. Cone, T. Chanelière, S. Kröll, S. A. Moiseev, and M. Sellars, Laser Photon. Rev. **4**, 244 (2010).

[21] B. Lauritzen, J. Minář, H. de Riedmatten, M. Afzelius, and N. Gisin, Phys. Rev. A **83**, 012318 (2011).

[22] T. Böttger, C. W. Thiel, R. L. Cone, and Y. Sun, Phys. Rev. B **77**, 155125 (2008).

[23] C. Li, C. Wyon, and Richard Moncorge, IEEE J. Quant. Elect. **28**, 1209 (1992).

[24] B. A. Maksimov, Yu. A. Kharitonov, V. V. Ilyukhin, and N. B. Belov, Sov. Phys. Dokl. **13**, 1188 (1969) [Doklady Akademii Nauk SSSR **183**, 1072 (1968)].

[25] Y. Sun and R. L. Cone (unpublished).

[26] Y. Sun, T. Böttger, C. W. Thiel, and R. L. Cone, Phys. Rev. B **77**, 085124 (2008).

[27] R. Beach, M. D. Shinn, L. Davis, R. W. Solarz, and W. F. Krupke, IEEE J. Quant. Elect. **26**, 1405 (1990).

[28] V. Crozatier, G. Gorju, F. Bretenaker, J.-L. Le Gouët, I. Lorgeré, O. Guillot-Noël, and Ph. Goldner, J. Lumin. **127**, 65 (2007).

[29] R. Krishna Mohan, T. Chang, M. Tian, S. Bekker, A. Olson, C. Ostrander, A. Khallaayoun, C. Dollinger, W. R. Babbitt, Z. Cole, R. R. Reibel, K. D. Merkel, Y. Sun, R. L. Cone, F. Schlottau, and K. H. Wagner, J. Lumin. **127**, 116 (2007).

[30] A. M. Stoneham, Rev. Mod. Phys. **41**, 82 (1969).

[31] R. L. Ahlefeldt, W. D. Hutchison, and M. J. Sellars, J. Lumin. **130**, 1594 (2010).

[32] M. Mehring and J. Mende, Phys. Rev. A **73**, 052303 (2006).

[33] L. Allen and J. H. Eberly, *Optical Resonance and Two Level Atoms* (Dover, New York, 1987).

[34] M. D. Levenson and S. S. Kano, *Introduction to Nonlinear Laser Spectroscopy* (Academic, New York, 1988).

[35] Y. Sun, C. W. Thiel, and R. L. Cone, Phys. Rev. B **85**, 165106 (2012).

[36] D. S. Sumida and T. Y. Fan, Opt. Lett. **19**, 1343 (1994).

[37] B. Herzog and E. L. Hahn, Phys. Rev. **103**, 148 (1956).

[38] J. R. Klauder and P. W. Anderson, Phys. Rev. **125**, 912 (1962).

[39] W. B. Mims, Phys. Rev. **168**, 370 (1968).

[40] P. Hu and S. R. Hartmann, Phys. Rev. B **9**, 1 (1974).

[41] W. B. Mims, in *Electron Paramagnetic Resonance*, edited by S. Geschwind (Plenum, New York, 1972), Chap. 4.

[42] D. Grischkowsky and S. R. Hartmann, Phys. Rev. B **2**, 60 (1970).

[43] W. B. Mims, Phys. Rev. B **5**, 2409 (1972).

[44] W. B. Mims, Phys. Rev. B **6**, 3543 (1972).

[45] L. Q. Lambert, Phys. Rev. B **7**, 1834 (1973).

[46] C. W. Thiel, R. M. Macfarlane, T. Böttger, Y. Sun, R. L. Cone, and W. R. Babbitt, J. Lumin. **130**, 1603 (2010).

[47] A. K. Rebane, C. W. Thiel, R. K. Mohan, and R. L. Cone, Bull. Russ. Acad. Sci. **74**, 934 (2010).

[48] O. Guillot-Noël, H. Vezin, Ph. Goldner, F. Beaudoux, J. Vincent, J. Lejay, and I. Lorgeré, Phys. Rev. B **76**, 180408(R) (2007).

[49] D. E. McCumber and M. D. Sturge, J. Appl. Phys. **34**, 6 (1963).

[50] A. M. Portis, Phys. Rev. **104**, 584 (1956).

[51] R. M. Macfarlane, R. Wannemacher, D. Boye, Y. P. Wang, and R. S. Meltzer, J. Lumin. **48-49**, 313 (1991).

[52] Y. P. Wang, D. P. Landau, R. S. Meltzer, and R. M. Macfarlane, J. Opt. Soc. Am. B **9**, 946 (1992).

[53] G. K. Liu, M. F. Joubert, R. L. Cone, and B. Jacquier, J. Lumin. **38**, 34 (1987).

[54] J. Huang, J. M. Zhang, A. Lezama, and T. W. Mossberg, Phys. Rev. Lett. **63**, 78 (1989).

[55] G. K. Liu and R. L. Cone, Phys. Rev. B **41**, 6193 (1990).

[56] F. R. Graf, A. Renn, G. Zumofen, and U. P. Wild, Phys. Rev. B **58**, 5462 (1998).